Journal of
Applied Crystallography

ISSN 0021-8898

Received 8 December 2009
Accepted 10 March 2010

Long-range ordering in anodic alumina films: a microradian X-ray diffraction study

Kirill S. Napolskii,[a]* Ilya V. Roslyakov,[a] Andrey A. Eliseev,[a] Andrei V. Petukhov,[b] Dmytro V. Byelov,[b] Natalia A. Grigoryeva,[c] Wim G. Bouwman,[d] Alexey V. Lukashin,[a] Kristina O. Kvashnina,[e] Andrey P. Chumakov[f] and Sergey V. Grigoriev[f]

[a]Department of Materials Science, Moscow State University, Leninskie Hills, 119992 Moscow, Russian Federation, [b]Van't Hoff Laboratory for Physical and Colloid Chemistry, Debye Institute for Nanomaterials, University of Utrecht 8, 3584 CH Utrecht, The Netherlands, [c]St Petersburg State University, 198504 St Petersburg, Russian Federation, [d]Delft University of Technology, Mekelweg 15, 2629 JB Delft, The Netherlands, [e]DUBBLE CRG/ESRF, The Netherlands Organization for Scientific Research, ESRF, BP 220, F-38043 Grenoble Cedex, France, and [f]St Petersburg Nuclear Physics Institute, Gatchina, 188300 St Petersburg, Russian Federation. Correspondence e-mail: napolsky@inorg.chem.msu.ru

A quantitative analysis of long-range order in the self-organized porous structure of anodic alumina films has been performed on the basis of a microradian X-ray diffraction study. The structure is shown to possess orientational order over macroscopic distances larger than 1 mm. At the same time, the interpore positional order is only short-range and does not extend over more than ~10 interpore distances. These positional correlations are mostly lost gradually rather than at the domain boundaries, as suggested by the divergence of the peak width for the higher-order reflections. In the direction of the film growth the pores have a very long longitudinal self-correlation length of the order of tens of micrometres.

1. Introduction

Self-organization of pores formed during anodization of metals in acidic media into periodic hexagonal structures has opened many new areas of application of anodic aluminium oxide (AAO) films as high-density data storage devices, calibration gratings, position-sensitive detectors with extremely high resolution and two-dimensional photonic crystals (Choi, Luo *et al.*, 2003; Masuda, 2006; Napolskii *et al.*, 2007; Nielsch *et al.*, 2001; Shingubara, 2003). It is generally believed that the origin of the self-organization of pores into a hexagonal network is the mechanical stress that is induced by the volume expansion of the aluminium during oxide growth (Houser & Hebert, 2009; Jessensky *et al.*, 1998). However, this still remains debated and an alternative mechanism has recently been proposed on the basis of electrochemical and symmetry assumptions (Su & Zhou, 2008).

The discovery of the two-step anodization technique (Masuda & Fukuda, 1995; Masuda & Satoh, 1996) and the hard anodization process (Lee *et al.*, 2006; Schwirn *et al.*, 2008) made a breakthrough in the preparation of polydomain porous alumina structures with narrow pore-size distributions and extremely high aspect ratios. Monodomain porous structures can be obtained by pre-patterning the aluminium substrates before anodization, which leads to pore nucleation in the appropriate predefined positions and guides the growth of the pores during anodization (Choi, Nielsch *et al.*, 2003; Masuda *et al.*, 1997). The interpore distance (D_{int}) can easily be varied by varying the applied voltage (Nielsch *et al.*, 2002; O'Sullivan & Wood, 1970; Shingubara *et al.*, 1997). However, self-organization occurs only in a rather narrow range of the anodization potential (Nielsch *et al.*, 2002), which greatly restricts the variation of D_{int}. A similar restriction holds in the case of nano-imprint technology, as the use of anodization voltages outside the self-organization window leads to a rapid perturbation of the pore ordering. By varying both the electrolyte composition and the anodization voltage one can vary D_{int} over a broader range (Li *et al.*, 2007; Nielsch *et al.*, 2002).

The vast majority of the reported structural investigations of AAOs have been based solely on electron microscopy (EM), which allows for fast and easy visualization of the surface structure on the two sides of the porous film. However, EM is able to access the structure only within a limited area and can provide data with limited statistics. It therefore possesses significant limitations for quantitative determination of long-range order. Moreover, the bulk structure can only be qualitatively addressed by cleaving the AAO membranes. A quantitative analysis of domain size on the basis of EM results was reported by Nielsch *et al.* (2002), but the results were not supplemented by information on the used definition of the domain. Furthermore, the dependencies of the average domain size *versus* the anodization time reported by different authors contradict each other (see, for example, Li *et al.*, 1998; Nielsch *et al.*, 2002).

The complications of the accurate determination of long-range ordering in AAO structures can be overcome using diffraction techniques, which provide information averaged over macroscopically large sample volumes. To the best of our knowledge, there are only a few works (Benfield, Dore *et al.*, 2004; Benfield, Grandjean *et al.*, 2004; Dore *et al.*, 2002; Lagrene & Zanotti, 2007) dealing with diffraction studies of the porous structure of anodic alumina films. In all these cases, porous membranes with disordered structures were used. Here, we report the results of a microradian X-ray diffraction study of the porous structure of AAO membranes obtained by two-step anodization in oxalic and sulfuric acids at 40 and 25 V, respectively. The anodization conditions were chosen within the self-organization window, and have been shown (Nielsch *et al.*, 2002) to be successful for the preparation of well ordered porous structures with periodicities of about 105 and 65 nm. We show that combining scanning electron microscopy (SEM) and high-resolution microradian X-ray diffraction allows us to determine accurately and quantitatively a number of long-range order parameters which cannot be measured by conventional microscopy techniques.

2. Experimental

2.1. Sample preparation

High-purity aluminium foil (99.999%, 0.5 mm thick, Goodfellow) was used as the starting material. Prior to anodization, the aluminium was annealed at 823 K in air for 12 h in order to remove mechanical stress and to enlarge the grain size in the metal. Subsequently, the foils were mechanically polished by diamond suspensions (Struers) to a mirror finish and cleaned repeatedly with acetone and deionized water in an ultrasonic bath.

The aluminium oxidation was performed in a two-electrode cell at a constant voltage of 40 V in 0.3 *M* oxalic acid [$(COOH)_2$, 98%, Aldrich] or 25 V in 0.3 *M* sulfuric acid (H_2SO_4, 95–97%, Fluka). Pt wire was used as the counter-electrode. The temperature of the electrolyte was kept in the range 273–274 K. After the first anodization, for 72 and 24 h in oxalic and sulfuric acid, respectively, the alumina film was selectively etched away in a 0.6 *M* H_3PO_4 + 0.2 *M* CrO_3 solution at 343 K. After the second anodization under the same conditions for 24 h, we obtained oxide films with thicknesses exceeding 50 µm.

2.2. Sample characterization

Diffraction experiments were performed at the Dutch–Belgian beamline BM-26 DUBBLE (Borsboom *et al.*, 1998; Bras *et al.*, 2003) of the European Synchrotron Radiation Facility (ESRF) in Grenoble (France) using a microradian X-ray diffraction setup similar to that described by Petukhov *et al.* (2006). A 13 keV X-ray beam was used (wavelength λ = 0.95 Å, bandpass $\Delta\lambda/\lambda = 2 \times 10^{-4}$). To improve the angular resolution of the setup, one has to increase the transverse coherence length l_{tr} of the beam at the sample position (Als-Nielsen & McMorrow, 2000). With a source size of about σ = 100 µm at the ESRF, values of the order of $l_{tr} = D\lambda/\sigma = 50$ µm can be achieved at the sample position located at D = 50 m from the source if beam focusing is avoided. Instead, the beam was focused by a set of beryllium compound refractive lenses (Snigirev *et al.*, 1996) installed in the experimental hutch just in front of the sample. The lenses focused the beam on the phosphor screen of a CCD-based two-dimensional detector (Photonic Science, 4008 × 2672 pixels of 22 × 22 µm). The beam focusing was tuned by adjusting the X-ray photon energy, which affects the focal distance of the lenses. The detector was installed at a distance of 8 m from the sample position. This scheme, which differs from an ordinary small-angle X-ray scattering setup by its novel approach to beam focusing, is especially suitable for X-ray diffraction studies of large-scale periodic structures and allows an angular resolution of about 5–10 microradian to be achieved. The sample was mounted on a goniometer head to allow for careful orientation around the horizontal and vertical axes orthogonal to the beam. The beam size at the sample was about 0.5–1 mm.

To investigate the surface texture of the Al foils, electron backscatter diffraction (EBSD) patterns were recorded employing a JEOL JSM-840A scanning electron microscope equipped with a NordlysS EBSD detector (Oxford Instruments). Surface analysis of the oxide films was carried out on a QuantaChrome NOVA 4200E instrument using N_2 as the working gas at 77 K. SEM images of the AAO porous films were recorded by a LEO Supra 50 VP instrument. Samples for SEM were covered with a thin conductive layer of carbon using a Scancoat sputterer (Edwards).

3. Results and discussion

According to the SEM observations, the obtained anodic alumina membranes possess a porous structure with uniform pores aligned perpendicular to the film surface (Fig. 1). The pores form a two-dimensional hexagonal structure with an interpore distance (D_{int}) of about 105 nm, which is typical for the applied anodization conditions [0.3 *M* $(COOH)_2$, 40 V; Nielsch *et al.*, 2002]. The SEM images suggest that the structure consists of apparent domains separated by boundaries that possess much greater deviation from the hexagonal ordering. Moreover, within every domain numerous point defects and dislocations can be observed, even after long anodization (see insets in Fig. 1*b*). Both the domain boundaries and the point defects can introduce disturbance of the structure. They can affect the pore positions and can lead to deformation of the pores themselves.

At first sight, the top (Fig. 1*a*) and bottom (Fig. 1*b*) parts of the porous membrane look similar. The porous structure contains disoriented domains with an average size of several micrometres. On the other hand, fast Fourier transform (FFT) images obtained from an area of about 60 µm^2 reveal a substantial difference (see insets in Fig. 1). The Fourier transform of the SEM image of the top surface of the membrane exhibits only intensity rings. The uniform distribution of intensity along the rings corresponds to complete disorientation of separate regions contributing to the FFT

pattern. In contrast, wide maxima instead of rings are clearly observed for the FFT image obtained from the bottom part of the membrane. This indicates that, during pore growth, orientational order is built over distances larger than the image size. In order to characterize quantitatively the long-range ordering parameters of the AAO structure, X-ray diffraction experiments were performed. A sketch of the geometry of the diffraction experiment is shown in Fig. 2.

An example of a microradian X-ray diffraction pattern recorded at normal incidence of the beam to the surface of an anodic alumina film obtained by the two-step anodization

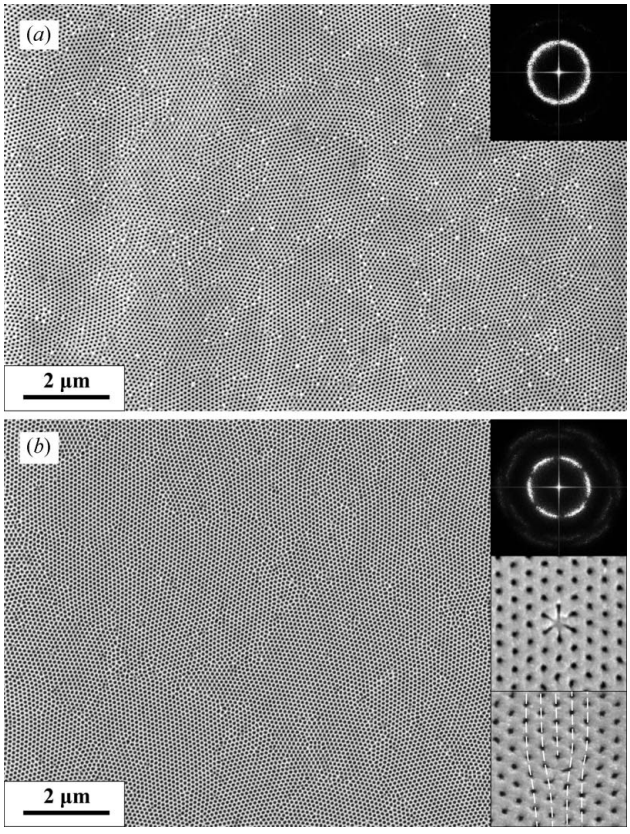

Figure 1
SEM images of anodic alumina film. (*a*) Top and (*b*) bottom of an AAO membrane after the second anodization [40 V, 0.3 *M* $(COOH)_2$]. The bottom view was obtained after removal of the barrier layer by chemical etching. The insets display the intensity of the Fourier transforms of the corresponding images. SEM images of a point defect and a dislocation within the ordered regions are shown in the middle and bottom insets of panel (*b*).

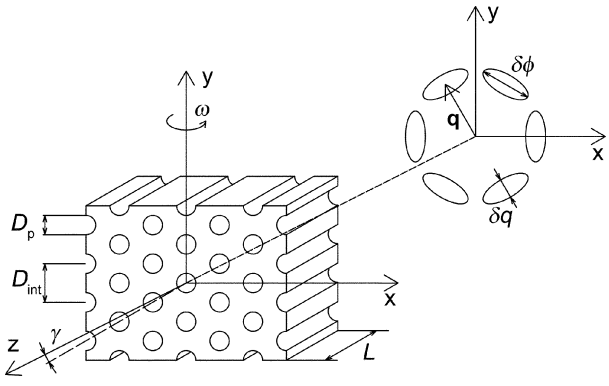

Figure 2
A sketch of the geometry of the diffraction experiment. The symbols are explained in the text.

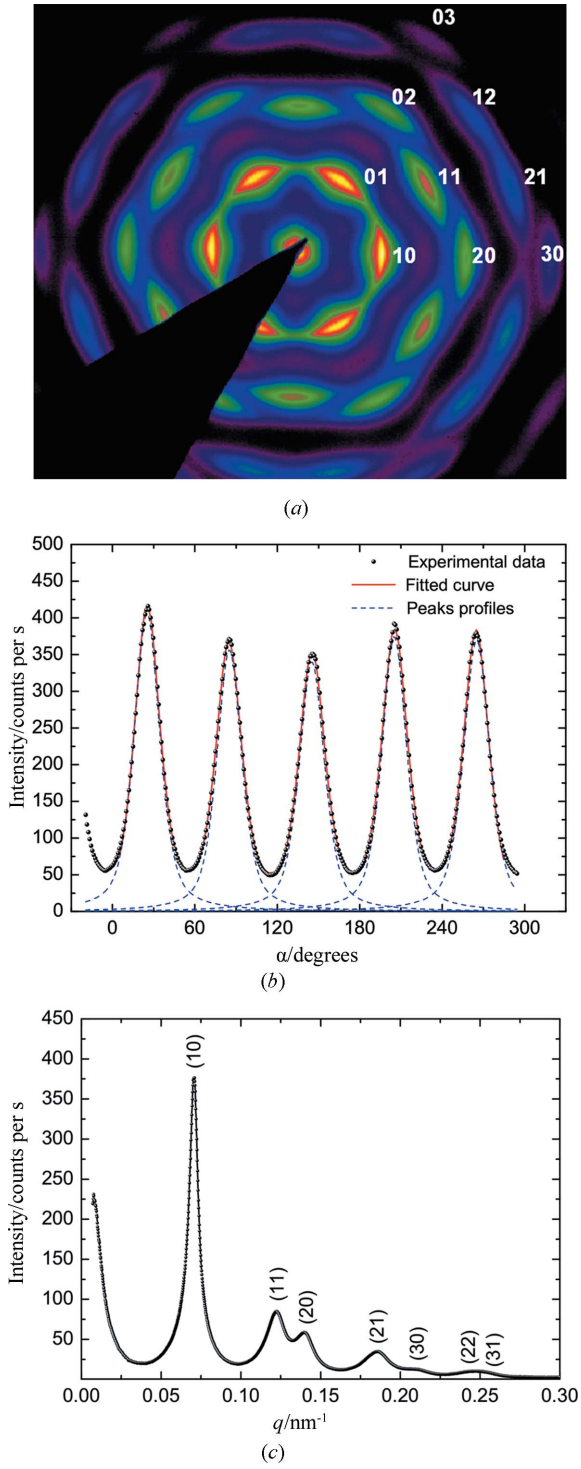

Figure 3
(*a*) Microradian diffraction pattern from an alumina membrane with an ordered porous structure obtained in oxalic acid at 40 V. The *hk* indices for a number of reflections are given. (*b*) The azimuthal variation of the intensity for the most intense (10) reflections. (*c*) The *q* dependence of the scattered intensity.

technique is presented in Fig. 3. According to EBSD data, the annealed aluminium foil contains single-crystal grains with a size of several millimetres in the lateral directions, their thickness being equal to the foil thickness. Taking into account the size of the irradiated area (0.5 × 0.5 mm), we can suppose that these diffraction patterns are obtained from the oxide film grown on a single-crystal substrate. In this case, the influence of grain boundaries on pore ordering in the oxide film (Grigor'ev *et al.*, 2007) is negligible.

The observed reflections form a hexagonal lattice, which can be generated using two basis vectors making an angle of 60° with each other and having a length of $b_1 = b_2 = 4\pi/(3^{1/2}D_{\rm int})$, where $D_{\rm int}$ is the interpore distance. The single-domain-like appearance of the diffraction pattern indicates that the orientational order extends over distances larger than the size of the irradiated area. Moreover, our recent results obtained using small-angle neutron scattering testify that even at a beam size of 8 mm the spot-like diffraction pattern can be observed (Grigor'ev *et al.*, 2007). Thus, the two-step anodization technique allows us to prepare AAO membranes with a very high degree of orientational order and homogeneity of the porous oxide films on a scale of up to a centimetre. At the same time, this does not mean that the structures of AAO films should be interpreted in terms of a single crystal with periodicity extending all over the illuminated area. More precisely, the structure of AAO can be represented as a set of domains oriented around a certain direction, giving sixfold symmetry in the diffraction pattern. Indeed, the diffraction maxima are significantly broadened in the azimuthal direction as a result of fluctuations of the orientational order. After integrating the peak intensity within a narrow q range around q_{10} ($q = 4\pi\sin\theta/\lambda$; 2θ is the diffraction angle), the azimuthal intensity profiles were determined as shown in Fig. 3(*b*). The Bragg-peak broadening in the azimuthal direction corresponds to the average spread of domain orientations of $\delta\phi_{10,\ \rm oxalic} = 22.3\ (5)^\circ$.

We have noticed that the diffraction patterns are extremely sensitive to sample orientation. Rotation of the sample by as little as 0.1° around the axes orthogonal to the beam leads to a significant modification of the diffraction pattern. Similar behaviour has been reported previously by Benfield, Dore *et al.* (2004) and Dore *et al.* (2002). Fig. 4 presents the rocking curve for the intensity of the 10 and $\bar{1}0$ diffraction peaks. Each point on the experimental curve represents the integral intensity of a diffraction peak obtained from the Lorentzian fit of the radial distribution of the scattered intensity $I(q)$. The curvature of the Ewald sphere is extremely small in the conditions of our experiment, owing to the small value of the diffraction angle 2θ. Still, because of the sharpness of the reflections in the direction parallel to the beam, the curvature of the Ewald sphere produces a clearly visible effect in Fig. 4. The rocking curves for the 10 and $\bar{1}0$ diffraction peaks are shifted by about 0.06°, *i.e.* by the diffraction angle 2θ. The width of the rocking curve $\delta\omega$ is related to the correlation length of the porous structure along the pores (L_z) *via* the equation

$$L_z = \frac{2\pi}{\delta q_z} = \frac{2\pi}{q_{10}\sin\delta\omega}, \qquad (1)$$

where δq_z is the width of the 10 diffraction maximum along the beam, q_{10} is the scattering vector corresponding to the 10 diffraction peak and $\delta\omega$ is the full width at half-maximum (FWHM) of the rocking curve. Using $\delta\omega = 0.52^\circ$ and $q_{10} = 0.07\ {\rm nm}^{-1}$, one can obtain $\delta q_z = q_{10}\sin\delta\omega = 6.35 \times 10^{-4}\ {\rm nm}^{-1}$, and in real space $L_z = 2\pi/\delta q_z = 10\ \mu{\rm m}$. In other words, the pores have a very long longitudinal self-correlation length, of the order of tens of micrometres. Here, we define the longitudinal self-correlation length as the length along the pore within which the difference between the pore and a best-fit straight cylinder is smaller than the pore diameter.

It is instructive to consider possible artifacts that can affect the above-described determination of the longitudinal self-correlation length of the pores. For example, the beam coherence in the longitudinal direction is determined by the spectral width $\Delta\lambda$ of the radiation. In the conditions of the present experiment ($\lambda = 0.95$ Å and $\Delta\lambda/\lambda = 2 \times 10^{-4}$), the longitudinal coherence length $l_{\rm long} = \lambda^2/\Delta\lambda$ is as short as 0.5 μm. The actual X-ray beam therefore consists of wave packets that are significantly shorter than the pores. However, this does not restrict the resolution of the rocking-curve measurements, since the actual length of coherent interaction in the longitudinal direction is determined by $l_{\rm long}/(2\sin^2\theta)$, where θ denotes half of the diffraction angle (Petukhov *et al.*, 2002). It is therefore clear that, in small-angle diffraction experiments, the finite monochromaticity can be simply neglected. A more serious restriction of resolution in the rocking-curve measurements is in fact related to the angular spread of the plane wave components (Petukhov *et al.*, 2004). For example, as a result of beam focusing by the lens installed in front of the sample, the phase fronts of the waves are slightly bent. The spread of the directions is governed by half of the lens aperture (less than 500 μm) divided by the lens–detector distance of about 8 m. This yields an angular spread of about 50 microradian or 0.003°, which is significantly

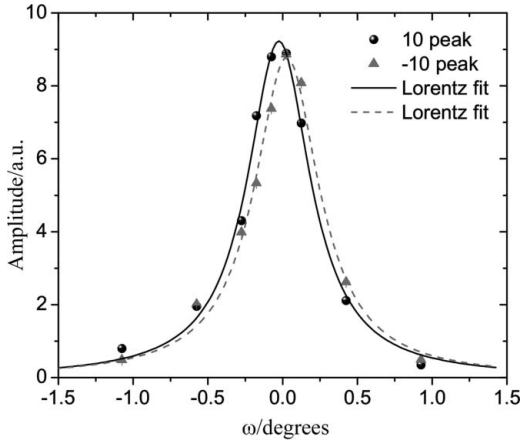

Figure 4
Rocking curves for the 10 (circles) and $\bar{1}0$ (triangles) Bragg reflections. The oxide film was prepared in 0.3 *M* oxalic acid at 40 V. The lines show the result of the Lorentz fit.

smaller than the experimentally determined value of $\delta\omega$, *i.e.* instrumental limitations do not affect the result.

Finally, we have to consider the possible effects of dynamic diffraction. A single pore of length L oriented along the beam will produce a phase shift of $\varphi = (2\pi/\lambda)L(1-n)$, where $n = 1 - 5.2 \times 10^{-6}$ is the refractive index of alumina under the conditions of the present experiment. At a distance $L = 10$ µm, the phase shift $\varphi \simeq \pi$. The kinematic approach, which assumes weak scattering, is only applicable for much smaller phase shifts. It is therefore clear that dynamic effects could become important (de Beer & Petukhov, 2007). The above estimate of the longitudinal self-correlation length L_z can therefore be considered as the lower limit of L_z.

In the radial direction the scattered intensity $I(q)$ (see Fig. 3*c*) is described by the general relation

$$I(q) \propto F(q)S(q), \tag{2}$$

where $F(q)$ and $S(q)$ are the form and structure factors, respectively. $F(q)$ is related to the shape of a single pore, while $S(q)$ describes the spatial arrangement of the pores. In comparison with colloidal systems, the experimental determination of the form factor in the case of scattering by the porous structure of anodic alumina films is highly obstructed. On the other hand, $F(q)$ can be calculated theoretically (Guinier & Fournet, 1955). The pores are trumpet-shaped, with a slight increase of the channel diameter in the upper part of the membrane due to chemical dissolution of the aluminium oxide in the acidic medium during the long anodization procedure (O'Sullivan & Wood, 1970). In order to simplify the calculations, the pores were approximated as polydisperse cylinders. Taking into account a pore-size distribution $h(r)$ and an orientation distribution function $g(\alpha)$, the average $F(q)$ can be calculated using the following equations:

$$F(q) \propto \iint g(\alpha)h(r)\,\frac{f^2(q,\alpha,r)\sin\alpha}{V_{\rm cyl}}\,{\rm d}\alpha{\rm d}r, \tag{3}$$

where

$$f(q,\alpha,r) = V_{\rm cyl}\,j_0\left(\frac{qL_{\rm cyl}\cos\alpha}{2}\right)\frac{J_1(qr\sin\alpha)}{(qr\sin\alpha)}, \tag{4}$$

$$V_{\rm cyl} = \pi r^2 L_{\rm cyl}, \tag{5}$$

$$j_0(x) = \sin(x)/x, \tag{6}$$

$J_1(x)$ is the first-order Bessel function, r, $L_{\rm cyl}$ and $V_{\rm cyl}$ are the radius, length and volume of the cylinder, respectively, and α is defined as the angle between the cylinder axis and the scattering vector **q**. The integral over α averages the form factor over all possible orientations of the cylinder with respect to **q**. The integral over r averages $F(q)$ over pores with various diameters.

The pore-size distribution function $h(r)$ can be estimated from SEM or adsorption measurements. According to SEM micrographs from the top surface of the oxide film (Fig. 5*a*), the pore diameter is $D_{\rm p} = 32.7$ (29) nm (see Fig. 5*b*). Data on more than 850 pores were treated to construct the pore-size distribution. Capillary adsorption data (Fig. 5*c*), recalculated using the Barret–Joyner–Halenda (BJH) approach (Barrett *et al.*, 1951), yield a smaller value for the average pore diameter and a higher polydispersity [$D_{\rm p} = 30.0$ (71) nm], which is not surprising given the trumpet-like shape of the channels. The errors are specified as the half-width at half-maximum (HWHM) of the corresponding pore-size distributions. Since the diffraction patterns are recorded in transmission mode, the mean values of the pore radius and polydispersity obtained from adsorption measurements have been used for the calculation of $F(q)$.

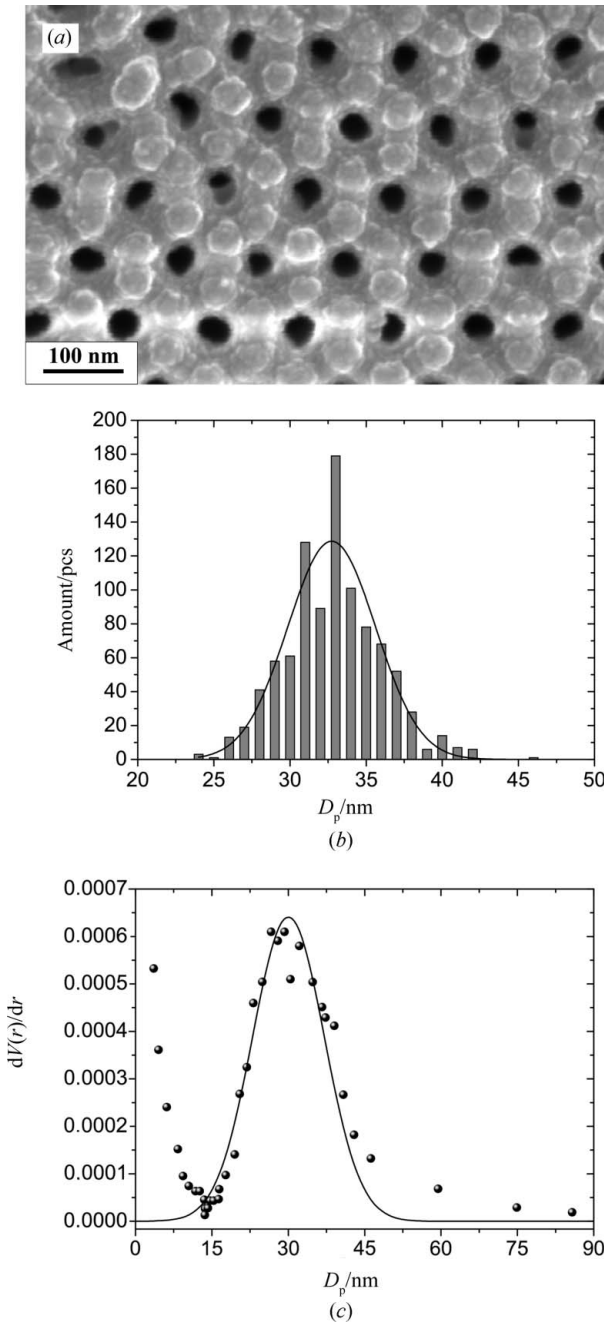

Figure 5
(*a*) Top view SEM micrograph of an anodic alumina film [40 V, 0.3 *M* $(COOH)_2$]. (*b*) Pore-size distribution calculated from SEM data and (*c*) from adsorption measurements. The solid lines are Gaussian fits to the experimental data.

The deviation of the magnitude of the (10) Bragg peaks from the mean value is less than 10% (see Fig. 3*b*). According to the rocking curves (Fig. 4), such a small variation in peak intensity indicates that the misalignment γ of the pore axis with respect to the X-ray beam is less than 0.1°. Consequently, as an orientation distribution function $g(\alpha)$ a Lorenzian with a centre at $\pi/2$ and a FWHM equal to the FWHM of the obtained rocking curve can be used.

The calculated form factor of 47% polydisperse cylinders with an average radius of 15 nm and a length of 10 µm at a nearly parallel ($\delta\omega = 0.52°$) orientation of the pores to the incident beam is shown in Fig. 6(*a*). The form factor is normalized such that $F(q \rightarrow 0) = 1$. There are no pronounced minima in the $F(q)$ curve, but at the same time it leads to a rapid decrease in the scattered intensity with increasing q.

Fig. 6(*b*) illustrates the structure factor [$S(q) = I(q)/F(q)$] normalized to the intensity of the 10 diffraction peak. The data were fitted to a sum of Lorentzians. As shown in Fig. 6(*b*), the result of the fit closely follows the experimental data. The fits yield the values of a number of parameters for every diffraction maximum, such as its intensity (I_{hk}), position (q_{hk}) and FWHM in the radial direction (δq_{hk}). In the following discussion, only the diffraction maxima at $q < 0.35$ nm^{-1} will be analysed, since the parameters of the higher-order reflections are sensitive to background subtraction details.

The observed peak positions at $q_{10} = 0.07107$ (2), $q_{11} = 0.12323$ (3), $q_{20} = 0.14095$ (3), $q_{21} = 0.18679$ (2), $q_{30} = 0.21091$ (5), $q_{22} = 0.2439$ (3), $q_{31} = 0.2540$ (3), $q_{40} = 0.2824$ (3), $q_{32} = 0.3064$ (6) and $q_{41} = 0.321$ (1) nm^{-1} correspond very well to hexagonal ordering of the pores and allow one to determine the periodicity with good accuracy. Refinement of the structure yields an interpore distance of $D_{\rm int} = 103.8$ (5) nm.

Before discussing the obtained peak widths, we should consider the possible effects of instrument resolution. To evaluate the latter, we have measured the profile of the direct beam (Fig. 7). The fit of these data yields an estimate of the FWHM of the instrumental function of $\Delta = 5.9\,(1) \times 10^{-4}$ nm^{-1}. For comparison, the radial profile of the 10 diffraction reflection for the AAO membrane obtained in oxalic acid is also shown in Fig. 7. One can see that, in spite of the rather large-scale periodicity of the structure, the microradian setup at DUBBLE is able to resolve the peak profile in great detail. The apparent peak width $\delta q_{\rm app}$ as determined from the fit was corrected for the instrument resolution Δ assuming the relation $(\delta q_{\rm app})^2 = \Delta^2 + (\delta q_{\rm intr})^2$, where $\delta q_{\rm intr}$ is the actual width of the reflections.

From the radial width δq_{10} of the lowest-order Bragg peak, we find that the positional correlations of the pores are rather short-range. They do not extend beyond $m = q_{10}/\delta q_{10} = 10$ lattice periods. The positional correlations can be lost not only at the domain boundaries but also within the domains, owing to the various types of lattice deformation. These two main types of positional disorder can be easily distinguished in the diffraction data. Domain boundaries usually lead to a sudden loss of positional correlations. As a result, all diffraction orders broaden in the same way by an amount inversely proportional to the domain size. On the other hand, lattice deformations (*e.g.* caused by microstrain) lead to a monotonic decay of positional correlations. As a result, higher-order diffraction peaks, which correspond to smaller-scale periodi-

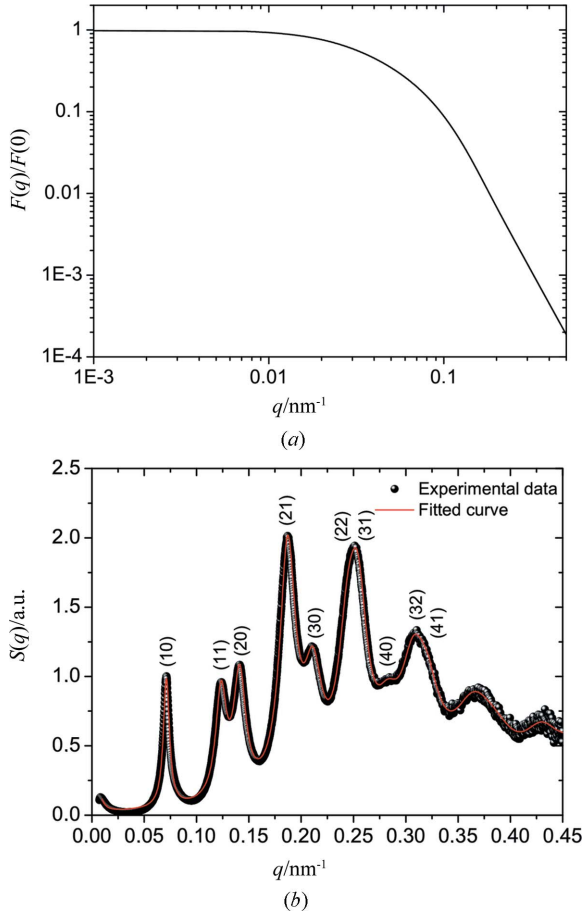

Figure 6
(*a*) Form factor of pores in an anodic alumina film obtained in oxalic acid at 40 V. (*b*) Structure factor. The solid line displays the result of fitting the experimental data to a sum of Lorentzians.

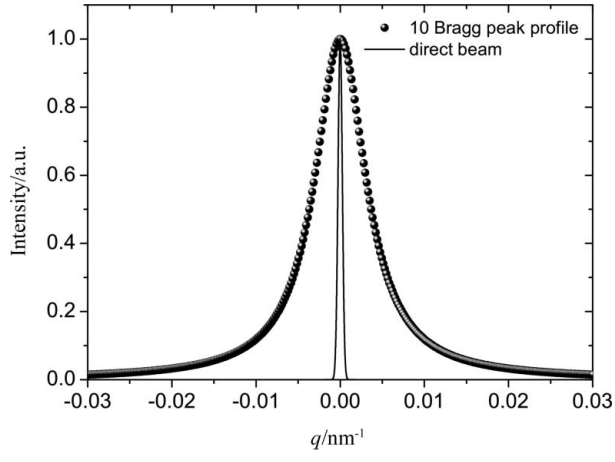

Figure 7
The radial profile of the 10 diffraction peak, along with the instrumental resolution (solid line). Data for the porous film obtained in oxalic acid at 40 V. For comparison, the centres of the peaks are displaced to zero.

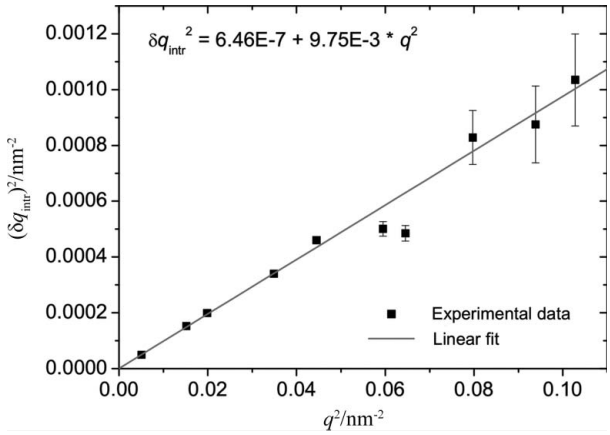

Figure 8
The square of the radial intrinsic width $(\delta q_{hk})^2$ of the different order reflections as a function of q^2. The line is the linear fit to the experimentally observed widths of the reflections.

city, broaden more than the low-order diffraction peaks (Guinier, 1994; Pecharsky & Zavalij, 2003).

Since a finite crystallite size (Λ) and microstrain (ε) yield statistically independent contributions to the reflection width $\delta q_{\rm intr}$, we may assume that

$$\delta q_{hk}^2 = \delta q_0^2 + (k\varepsilon q)^2, \qquad (7)$$

where k is a constant that depends on the definition of a microstrain.

The experimentally observed squared values of the radial intrinsic widths of the Bragg peaks as a function of q^2 fit perfectly by linear dependance, with $\delta q_0^2 = 6.5\,(91) \times 10^{-7}$ nm^{-2} and a slope $(k\varepsilon)^2$ of 9.75 (8) $\times 10^{-3}$ (see Fig. 8). The typical size of the domains can be estimated as $\Lambda = 2\pi B/\delta q_0$, where B is a factor of the order of 1, which depends on the domain shape. Using $B = 1$, one obtains $\Lambda = 8$ µm. We note that this value is close to the apparent domain size in the SEM images (Fig. 1). At the same time, accurate determination of the small intercept value δq_0^2 in Fig. 8 is difficult since it depends sensitively on a small variation in the experimentally determined values. Our results show that the contribution of microstrain to the broadening of the Bragg peaks is much larger than the finite size effect, even for the lowest-order reflections. The interpore positional order is therefore mostly lost within the domains rather than at the domain boundaries. This means that, if a higher degree of positional order is needed in AAO membranes, one needs first of all to improve the ordering of the pores within the domains rather than attempting to increase the domain size.

The protocol for the treatment of diffraction data described in detail above is general and can be easily applied for the structural characterization of anodic oxide films with various periodicity and structure quality. In the case of the anodization of aluminium in 0.3 M sulfuric acid at 25 V, a periodicity of 65.0 (2) nm was found. The mosaicity of the obtained film is $\delta\phi_{10,\,\rm sulfuric} = 26.0\,(8)^\circ$ and the longitudinal self-correlation length in the direction normal to the film surface is $L_{z,\,\rm sulfuric} = 2\pi/\delta q_z \simeq 13$ µm.

Since the diffraction patterns are obtained in transmission mode, the above-mentioned characteristics of Al_2O_3 porous films, such as structure periodicity, pore misorientation, size of domains and domain disorientation, are in fact averaged values for the structure of anodic alumina through the whole thickness of the membrane. These sorts of data can not be obtained using conventional microscopy techniques, which only give information on the surface of the sample. Since the top and bottom parts of the AAO film have the most disordered and the most ordered structures, respectively, the determination of averaged parameters of the AAO structure may be of great interest in membrane characterization.

4. Conclusions

We have demonstrated that microradian X-ray diffraction is an excellent tool for the structural characterization of self-ordered porous oxide films. In contrast to conventional microscopy techniques, the approach presented here allows quantitative determination of the ordering of self-organized AAO structures. We have found that the orientational correlations extend over macroscopic distances greater than 1 mm. At the same time, significant fluctuations of the orientations are present. In contrast, the interpore positional order is rather short-range and does not extend beyond ~10 periods. The diverging width of the higher-order reflections suggests that the positional correlations are lost gradually, presumably as a result of a high density of dislocations and other sources of lattice distortions. In the direction of film growth, the pores have a very long self-correlation length of the order of tens of micrometres.

Application of the suggested approach to the study of the influence of preparation conditions on long-range ordering in AAO films will be the subject of further work.

This work was partially supported by the Federal Agency of Science and Innovations (grant Nos. 02.513.11.3485 and 02.513.11.3488) and the Russian Foundation for Basic Research. We thank the personnel of the DUBBLE beamline, and in particular D. Detollenaere, for their excellent support. The authors are grateful to A. Snigirev (ESRF) for his help with X-ray optics and enlightening discussions. We thank A. Mankevich and A. Vyacheslavov for EBSD and adsorption measurements, respectively. The Nederlandse Organisatie voor Wetenschappelijk Onderzoek is thanked for granting us beam time.

References

Als-Nielsen, J. & McMorrow, D. (2000). *Elements of Modern X-ray Physics*. Chichester: Wiley and Sons.
Barrett, E. P., Joyner, L. G. & Halenda, P. H. (1951). *J. Am. Chem. Soc.* **73**, 373–380.
Beer, A. G. F. de & Petukhov, A. V. (2007). *J. Appl. Cryst.* **40**, 144–150.
Benfield, R. E., Dore, J. C., Grandjean, D. & Kroll, M. (2004). *J. Alloys Compd.* **362**, 48–55.

Benfield, R. E., Grandjean, D., Dore, J. C., Esfahanian, H., Wu, Z., Kroll, M., Geerkens, M. & Schmid, G. (2004). *Faraday Discuss.* **125**, 327–342.
Borsboom, M., Bras, W., Cerjak, I., Detollenaere, D., Glastra van Loon, D., Goedtkindt, P., Konijnenburg, M., Lassing, P., Levine, Y. K., Munneke, B., Oversluizen, M., van Tol, R. & Vlieg, E. (1998). *J. Synchrotron Rad.* **5**, 518–520.
Bras, W., Dolbnya, I. P., Detollenaere, D., van Tol, R., Malfois, M., Greaves, G. N., Ryan, A. J. & Heeley, E. (2003). *J. Appl. Cryst.* **36**, 791–794.
Choi, J., Luo, Y., Wehrspohn, R. B., Hillebrand, R., Schilling, J. & Gosele, U. (2003). *J. Appl. Phys.* **94**, 4757–4762.
Choi, J., Nielsch, K., Reiche, M., Wehrspohn, R. B. & Gosele, U. (2003). *J. Vacuum Sci. Technol. B*, **21**, 763–766.
Dore, J. C., Benfield, R. E., Grandjean, D., Schmid, G., Kroll, M. & Le Bolloc'h, D. (2002). *Stud. Surf. Sci. Catal.* **144**, 163–170.
Grigor'ev, S. V., Grigor'eva, N. A., Syromyatnikov, A. V., Napol'skii, K. S., Eliseev, A. A., Lukashin, A. V., Tret'yakov, Y. D. & Eckerlebe, H. (2007). *JETP Lett.* **85**, 449–453.
Guinier, A. (1994). *X-ray Diffraction: In Crystals, Imperfect Crystals and Amorphous Bodies*. New York: Dover Publications.
Guinier, A. & Fournet, G. (1955). *Small-Angle Scattering of X-rays*. New York: John Wiley and Sons.
Houser, J. E. & Hebert, K. R. (2009). *Nat. Mater.* **8**, 415–420.
Jessensky, O., Muller, F. & Gosele, U. (1998). *Appl. Phys. Lett.* **72**, 1173–1175.
Lagrene, K. & Zanotti, J. M. (2007). *Eur. Phys. J. Spectrosc. Top.* **141**, 261–265.
Lee, W., Ji, R., Gosele, U. & Nielsch, K. (2006). *Nat. Mater.* **5**, 741–747.
Li, F., Zhang, L. & Metzger, R. M. (1998). *Chem. Mater.* **10**, 2470–2480.
Li, Y. B., Zheng, M. J. & Ma, L. (2007). *Appl. Phys. Lett.* **91**, 073109.
Masuda, H. & Fukuda, K. (1995). *Science*, **268**, 1466–1468.
Masuda, H. & Satoh, M. (1996). *Jpn. J. Appl. Phys.* **35**, L126–L129.
Masuda, H., Yamada, H., Satoh, M., Asoh, H., Nakao, M. & Tamamura, T. (1997). *Appl. Phys. Lett.* **71**, 2770–2772.
Masuda, M. Y. (2006). *Adv. Mater.* **18**, 213–216.
Napolskii, K. S., Eliseev, A. A., Yesin, N. V., Lukashin, A. V., Tretyakov, Y. D., Grigorieva, N. A., Grigoriev, S. V. & Eckerlebe, H. (2007). *Physica E*, **37**, 178–183.
Nielsch, K., Choi, J., Schwirn, K., Wehrspohn, R. B. & Gosele, U. (2002). *Nano Lett.* **2**, 677–680.
Nielsch, K., Wehrspohn, R. B., Barthel, J., Kirschner, J., Gosele, U., Fischer, S. F. & Kronmuller, H. (2001). *Appl. Phys. Lett.* **79**, 1360–1362.
O'Sullivan, J. P. & Wood, G. C. (1970). *Proc. R. Soc. London Ser. A*, **317**, 511–543.
Pecharsky, V. K. & Zavalij, P. Y. (2003). *Fundamentals of Powder Diffraction and Structural Characterization of Materials*. Dordrecht: Kluwer Academic Publishers.
Petukhov, A. V., Aarts, D. G., Dolbnya, I. P., De Hoog, E. H., Kassapidou, K., Vroege, G. J., Bras, W. & Lekkerkerker, H. N. (2002). *Phys. Rev. Lett.* **88**, 208301.
Petukhov, A. V., Dolbnya, I. P., Aarts, D. G. & Vroege, G. J. (2004). *Phys. Rev. E*, **69**, 031405.
Petukhov, A. V., Thijssen, J. H. J., 't Hart, D. C., Imhof, A., van Blaaderen, A., Dolbnya, I. P., Snigirev, A., Moussaïd, A. & Snigireva, I. (2006). *J. Appl. Cryst.* **39**, 137–144.
Schwirn, K., Lee, W., Hillebrand, R., Steinhart, M., Nielsch, K. & Gosele, U. (2008). *ACS Nano*, **2**, 302–310.
Shingubara, S. (2003). *J. Nanoparticle Res.* **5**, 17–30.
Shingubara, S., Okino, O., Sayama, Y., Sakaue, H. & Takahagi, T. (1997). *Jpn. J. Appl. Phys.* **36**, 7791–7795.
Snigirev, A., Kohn, V., Snigireva, I. & Lengeler, B. (1996). *Nature (London)*, **384**, 49–51.
Su, Z. X. & Zhou, W. Z. (2008). *Adv. Mater.* **20**, 3663–3667.